JGR Solid Earth

RESEARCH ARTICLE
10.1029/2021JB023136

Frictional Stability of Metamorphic Epidote in Granitoid Faults Under Hydrothermal Conditions and Implications for Injection-Induced Seismicity

Mengke An[1,2], Fengshou Zhang[1,2], Ki-Bok Min[3], Derek Elsworth[4,5], Changrong He[6], and Luanxiao Zhao[7]

[1]Department of Geotechnical Engineering, College of Civil Engineering, Tongji University, Shanghai, China, [2]Key Laboratory of Geotechnical & Underground Engineering of Ministry of Education, Tongji University, Shanghai, China, [3]Department of Energy Resources Engineering and Research Institute of Energy and Resources, College of Engineering, Seoul National University, Gwanak-ro 1, Seoul, Republic of Korea, [4]Department of Energy and Mineral Engineering, EMS Energy Institute and G3 Center, the Pennsylvania State University, University Park, PA, USA, [5]Department of Geosciences, the Pennsylvania State University, University Park, PA, USA, [6]State Key Laboratory of Earthquake Dynamics, Institute of Geology, China Earthquake Administration, Beijing, China, [7]State Key Laboratory of Marine Geology, Tongji University, Shanghai, China

Abstract The presence of metamorphic epidote on faults has been implicated in the transition from stable to unstable slip and the nucleation of earthquakes. We present structured laboratory observations of mixed epidote and simulated Pohang granodiorite (analogous to the EGS-enhanced geothermal system site) gouges to evaluate the impact of heterogeneity and contiguity of epidote-patch structure on frictional instability. Experiments are at a confining pressure of 110 MPa, pore fluid pressures of 42–63 MPa, temperatures 100–250°C and epidote percentages of 0–100 vol.%. The simulated Pohang granodiorite gouge is frictionally strong (friction coefficient ~0.71) but transits from velocity-strengthening to velocity-weakening at temperatures >150°C. This velocity-weakening effect is amplified in approximate proportion to increasing epidote content. Modes of epidote precipitation likely control the size and contiguity of the epidote-only patches and this in turn changes the response of 50:50 epidote-granodiorite mixed gouges for different geometric configurations. However, 50:50 epidote-granodiorite mixtures that are variously homogeneously mixed, encapsulated and checkerboarded in their structures are insensitive to their geometries – all reflect the high frictional strength and strong velocity-weakening response of 100:0 pure epidote. This suggests that the epidote present as thin coatings on fractures/faults can enhance velocity-weakening behavior, independent of individual patch size and can thereby support the potential seismic reactivation of faults. Considering the frictional and stability properties of epidote at conditions typical of shallow depths, the presence of low-grade metamorphism exerts a potentially important control on fault stability in granitoids with relevance as a marker mineral for susceptibility to injection-induced seismicity.

Plain Language Summary Epidote is a common mineral on fractures/faults in granites that results from both the natural and forced circulation of hot fluids – for example, in geothermal reservoirs. Its presence, even in trace quantities and as a film on fractures can impact the ability of faults to slip either stably or unstably – the latter generating earthquakes. We conduct shear experiments on simulated faults of powdered granodiorite gouge containing varying percentages and structures of epidote through pure epidote and at varying temperatures and pressures representative of geothermal reservoirs. The powdered granodiorite and epidote gouges show similar and high frictional strengths but the addition of epidote results in unstable slip and the potential for seismicity. Increasing epidote proportion amplifies the weakening until 50:50 mixtures that behave as unstably as pure epidote – regardless of the epidote-granite structure. This suggests that even trace amounts of epidote in thin films may be effective in destabilizing faults – with implications for the control of fault instability and earthquake triggering in geothermal reservoirs.

Key Points:

- Epidote gouge is more v-weakening than simulated gouge derived from the Pohang granite host above a transition T of ~150°C
- Homogeneous and structured 50:50 mixtures of epidote:granodiorite show v-weakening similar to epidote and are insensitive to structure
- Trace percentages of epidote present as thin coatings and even at small patch sizes are a potential factor controlling fault instability

Supporting Information:

Supporting Information may be found in the online version of this article.

Correspondence to:

F. Zhang,
fengshou.zhang@tongji.edu.cn

Citation:

An, M., Zhang, F., Min, K.-B., Elsworth, D., He, C., & Zhao, L. (2022). Frictional stability of metamorphic epidote in granitoid faults under hydrothermal conditions and implications for injection-induced seismicity. *Journal of Geophysical Research: Solid Earth*, *127*, e2021JB023136. https://doi.org/10.1029/2021JB023136

Received 6 SEP 2021
Accepted 5 MAR 2022

Author Contributions:

Methodology: Mengke An, Derek Elsworth
Validation: Mengke An, Fengshou Zhang
Writing – original draft: Mengke An
Writing – review & editing: Fengshou Zhang, Derek Elsworth, Changrong He, Luanxiao Zhao

1. Introduction

Fluid-injection-induced earthquakes associated with fluid-injection geoengineering activities are presently an important global concern for public safety and the integrity of infrastructure (Atkinson et al., 2020; Ellsworth, 2013; Majer et al., 2007; Schultz et al., 2020; Shapiro et al., 2006; Suckale, 2009). Massive fluid injection

may elevate fluid pressures and reactivate pre-existing fractures and faults and potentially trigger seismicity (Elsworth et al., 2016; Eyre et al., 2019; Guglielmi et al., 2015; McGarr et al., 2002). A better understanding of the mechanical, physical and chemical properties of deep fractures/faults is thus needed to mitigate this seismic hazard.

One type-example of this is the moment magnitude (M_w) 5.5 Pohang earthquake that occurred in November 2017 – one of the largest and most damaging earthquakes on the Korean peninsula since the last century (Grigoli et al., 2018; Kim et al., 2018). The event has attracted widespread attention not only for the significant resulting hazard and damage but also due to its connection with the Pohang EGS (enhanced geothermal system) project. This earthquake (Lee, Yeo, et al., 2019) directly injured >100 people and resulted in >US$300 million in economic loss. The event was likely triggered on an unmapped pre-existing critically-stressed fault reactivated at a depth of ∼3.8 km (see Figure S1 in Supporting Information S1) by the fluid injection during EGS stimulation (Lee, Yeo, et al., 2019). This earthquake is also the largest known injection-induced earthquake at an EGS site.

Two deep fluid-injection wells (i.e., PX-1 and PX-2 [Figure S1 in Supporting Information S1]) pierce the Pohang granodiorite to a depth of ∼4.2 km (Westaway & Burnside, 2019). Five hydraulic stimulations were conducted with a total injected volume of 12,798 m^3 and net injected volume of 5,841 m^3 considering bleed-off. Two months after the fifth hydraulic stimulation, on 15 November 2017, the M_w 5.5 Pohang earthquake occurred. Evidence for this seismicity correlating with fluid injection is apparent from the observed loss of drilling fluid, the spatio-temporal distribution of the seismic cloud and the numerical modeling (Ellsworth et al., 2019; Lee, Yeo, et al., 2019; Park et al., 2020; Yeo et al., 2020). During the vertical drilling of well PX-2 a significant loss (>160 m^3) of heavy drilling mud (1.60 g/cm^3) occurred in the depth range 3,816–3,840 m. This is immediately below the unmapped fault zone at depths of 3,790–3,816 m, indicating that well PX-2 transected the permeable unmapped fault zone.

The mechanical and physical properties of the subsurface fractures and faults are reflected in the subsurface core. A 3.6-m-length and 100-mm-diameter granodiorite core was recovered from geothermal well PX-2 in the depth range spanning 4,219–4,222.6 m (figure 3 in Kwon et al. (2019)) prior to hydraulic stimulation. The natural granodiorite fractures in Figure 1 were recovered from core samples of well PX-2 at a depth of ∼4,221 m.

SEM observations (Figure 1) of the natural granodiorite fracture show that typical minerals in the granodiorite include quartz, microcline, albite, and chlorite and are consistent with the mineral compositions of cuttings from PX-2 at depths of 3,535–3,814 m (table 2-1 of Lee, Yeo, et al. (2019)). In particular, the PX-2 cuttings at 3,535–3,814 m all contain chlorite, with the chlorite content spanning ∼5–19 wt.%. The natural granodiorite fracture plane (Figure 2) indicates the presence of epidote and chlorite. The chlorite occurs both in the granodiorite protolith and on the natural granodiorite fracture plane in Figure 2, while the epidote occurs only on the natural granodiorite fracture plane.

Epidote ($Ca_2FeAl_2[SiO_4][Si_2O_7]O(OH)$) is a common nesosilicate mineral that is widely distributed in the Earth's crust as a low-grade metamorphic mineral in pumpellyite-prehnite, greenschist, epidotite-amphibolite, and blueschist metamorphic facies (Bird & Spieler, 2004; Franz & Liebscher, 2004; Liou, 1993; Wehrens et al., 2016). In particular, epidote is also reported as distributed within granitoid fractures or veins where $T < 200$°C of active hydrothermal zones and has been observed at ∼100°C in several geothermal systems (e.g., Onikobe geothermal system of Japan; Bird & Spieler, 2004; Caruso et al., 1988; Kolawole et al., 2019). Fluids as transport media play an important role during the precipitation and growth of metamorphic epidote in granitoid fractures or faults at elevated temperatures (Kameda et al., 2011; Moore et al., 2001). And thus, the epidote can be regarded as an index mineral associated with the local temperature, permeability and fluid composition (Grapes & Hoskin, 2004; Hu et al., 2017). Previous experimental results show that epidote or epidotite gouge is frictionally strong, shows velocity-weakening behavior and promotes unstable fault slip at lower temperatures, generally at T (temperature) of ∼100–125°C (An et al., 2021; Fagereng & Ikari, 2020). Therefore, if the fluid-rock interactions under hydrothermal conditions contribute to the growth of epidote on fractures/faults, the epidote may control the response of the fracture or derivative gouge and therefore the frictional stability. In this case, the structure and contiguity of the hydrothermally precipitated patches will influence the stability of rupture and its manifestation as a seismic, rather than aseismic event.

Thus, we use powdered Pohang granodiorite, and the natural or laboratory-structured distribution of epidote therein, as a relevant type example to examine the effect of morphology of epidote gouge patches on the fault frictional response. In particular, we focus on the role of structure of the distributed epidote in controlling response.

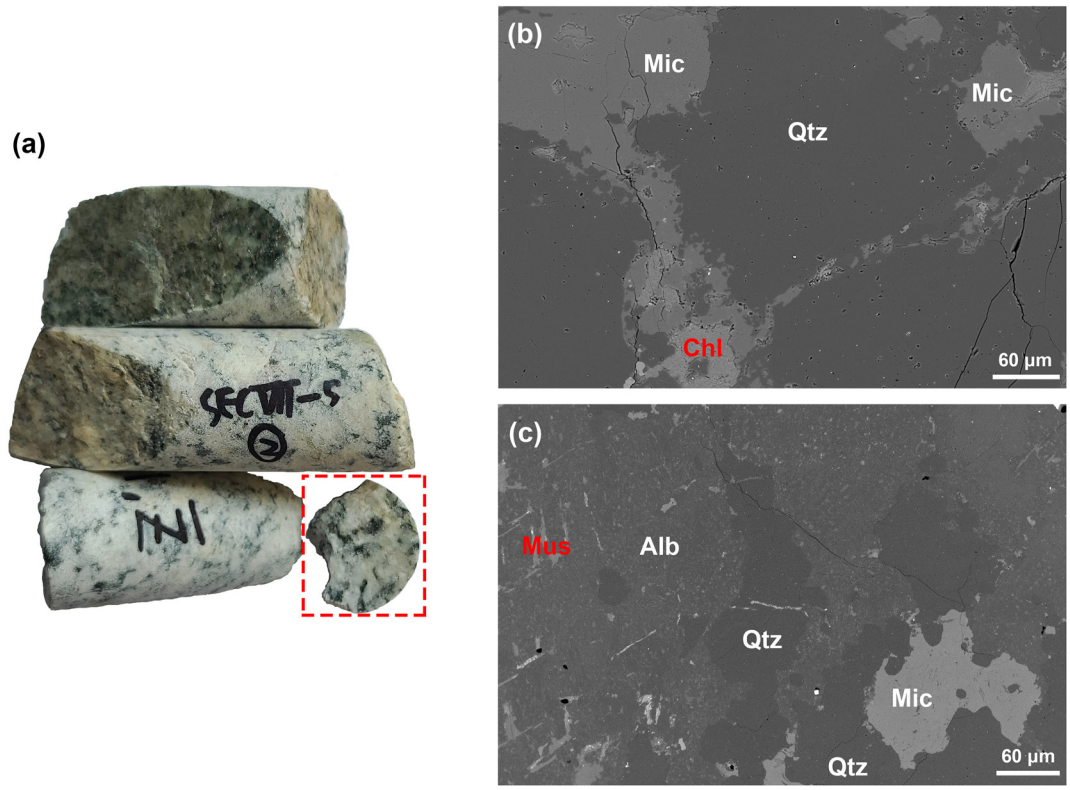

Figure 1. Photographs of (a) Pohang granodiorite rocks recovered from ~4.2 km depth prior to hydraulic stimulation and (b), (c) backscattered electron SEM (scanning electron microscopy) images. The SEM images of (b) and (c) were taken from the red dotted rectangle of (a). Typical minerals in Pohang granodiorite rocks include quartz (Qtz), microcline (Mic), albite (Alb), and chlorite (Chl).

We conduct shear experiments on powdered epidote, Pohang granodiorite rocks and mixtures thereof, to evaluate the frictional properties of these powdered rocks under hydrothermal conditions typifying a geothermal reservoir. We: (a) determine the frictional strength and stability of the powdered Pohang granodiorite gouge at different temperatures; (b) explore the variation of frictional properties of the simulated granodiorite gouge as a function of epidote content and structure; and (c) extrapolate the experimental results of the powdered granodiorite gouge to provide insight into the seismic behavior of faults under low-grade metamorphism.

2. Experimental Methods

2.1. Gouge Preparation

Unmetamorphosed Pohang granodiorite (Figure 1a) was used in our shear experiments. The gem-quality and short single crystal epidote (Figure S2 in Supporting Information S1) was collected from Handan city, Hebei, China. Both materials were crushed and then sieved to <75-μm diameter to simulate fault gouge. Mineral compositions of the two rock powders were analyzed using X-ray diffraction (XRD; apparatus type: D/max-rB) at Beidazhihui Micro Analytical Laboratory, Beijing, China with the results shown in the Supporting Information of An et al. (2021). The crystal epidote contains only trace inclusions (Figure S2 in Supporting Information S1) with the epidote gouge showing a >99 wt.% purity. The mixed and textured gouges were prepared from these two constituent gouges by adding them in different volume (vol.%) proportions and structures.

2.2. Experimental Procedure

We employed an argon-gas confined triaxial shear apparatus to conduct the fault friction experiments with a schematic of the apparatus shown in Figure 3 (He et al., 2006; Moore & Lockner, 2008, 2011). Detailed descriptions of the experimental apparatus are shown in Text T1 in Supporting Information S1.

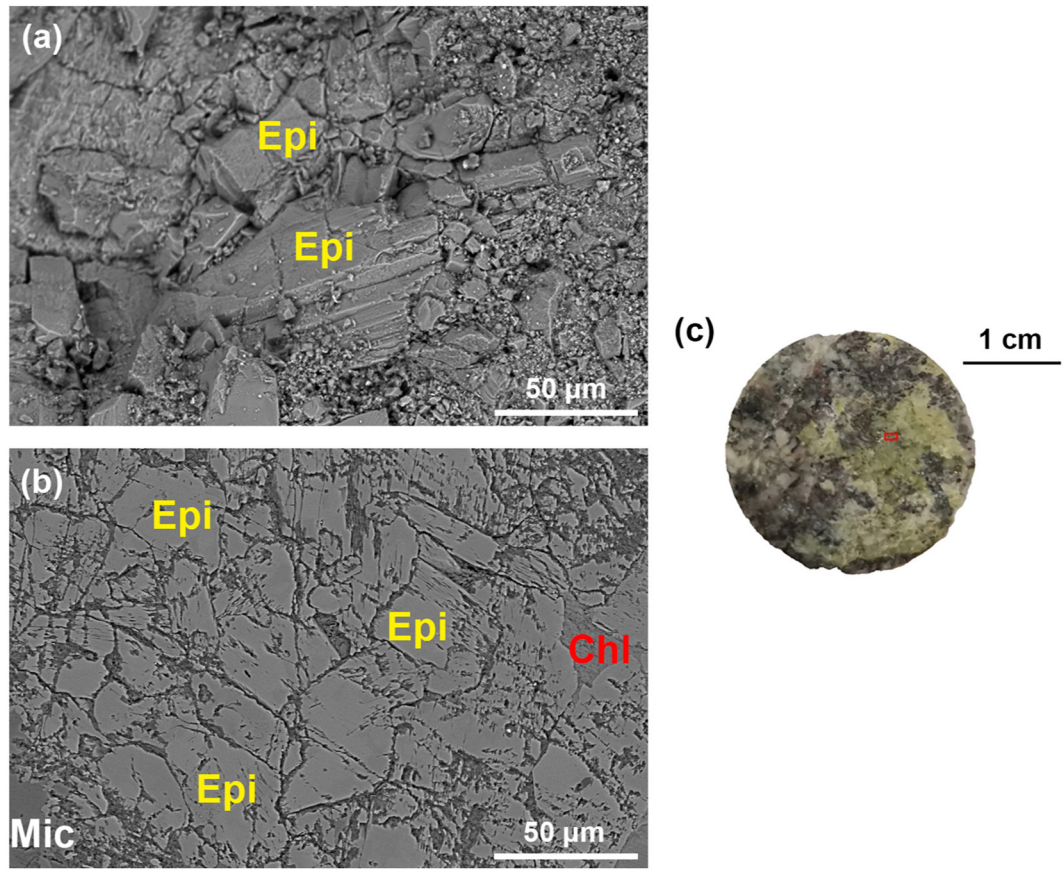

Figure 2. SEM photos showing the occurrence of metamorphic epidote on natural Pohang granodiorite fractures: (a) before polishing, and (b) after polishing. Both (a) and (b) are obtained at backscattered electron mode and from the red rectangle of (c). Short prismatic epidote crystals can be observed in (a). Epi = epidote, Chl = chlorite, Mic = microcline.

In our experiments, we mixed the simulated granodiorite gouge with an additional mass of powdered epidote in various proportions and spatial structures to investigate the effect of gouge texture and structure on fault frictional properties. For simplicity, we restrict our experiments to explore the frictional properties of 50 vol.% epidote and 50 vol.% granodiorite mixed gouge, only. Six different gouge structures are illustrated in Figure 4 to examine the impact of geometry, structure and size of gouge patch (epidote/granodiorite) on the mechanical response of the laboratory fault. We examine two structures of pure granodiorite (Gr) and epidote (Ep) gouges (Figure 4), one homogeneously mixed (HM) Gr + Ep gouge, encapsulated (EC) and then halved-checkerboard (2CQ) gouges and finally a quartered-checkerboard gouge (4CQ). This corresponds to a weight ratio of granodiorite:epidote of ~1:1.30. Gouge structures representing EC, 2CQ, and 4CQ were obtained by using steel shim masks cut to the various geometries.

A total of 12 shear experiments were conducted at a constant confining pressure (σ_c = 110 MPa), different pore fluid pressures (P_f = 42 and 63 MPa) and different temperatures (T = 100, 150, 200, and 250°C) for monomineralic gouges (granodiorite/epidote), uniformly mixed gouges (granodiorite:epidote = 50:50, 75:25, and 87.5:12.5) and different gouge structures (HM, EC, 2CQ, and 4CQ). Experimental details are listed in Table 1. The confining pressure σ_c = 110 MPa and pore fluid pressure P_f = 42 MPa correspond to the lithostatic and hydrostatic pressures at 4.2-km depth (assuming a rock density of 2,600 kg/m^3). A higher pore fluid pressure P_f = 63 MPa simulates the fluid injection conditions. The in-situ temperature at a depth of 4.2 *km* is estimated to be ~150°C (Westaway & Burnside, 2019). The selected depth of ~4.2 km corresponds to the location of the sampled granodiorite fractures in Figures 1 and 2 and approaching the depth of the mainshock hypocenter of the 15 November 2017 Pohang earthquake (Lee, Ellsworth, et al., 2019). The experiments (Table 1) can be classified into three groups according to the research objectives. The first group of experiments, including Gr-100, Gr-150, Gr-150-63, Gr-200, and Gr-250, were conducted at σ_c = 110 MPa, P_f = 42 or 63 MPa and incremented temperatures of

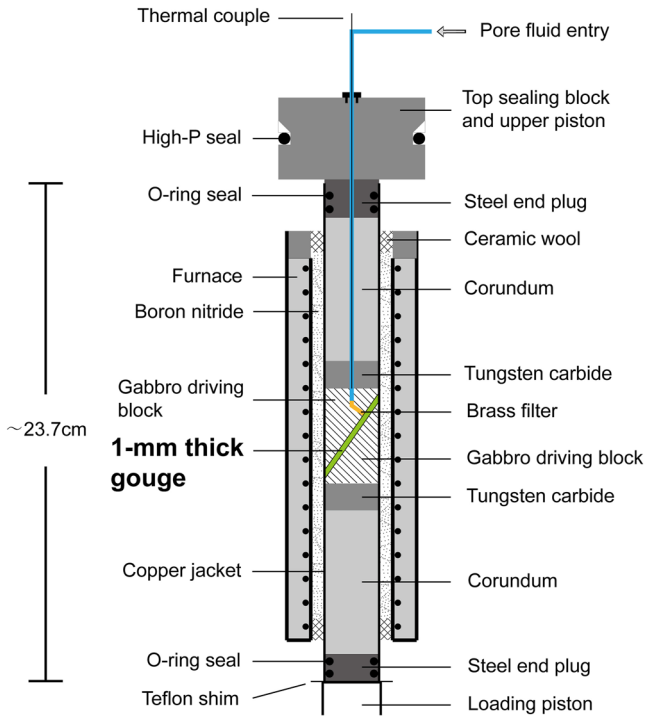

Figure 3. Experimental assembly.

100, 150, 200, and 250°C, to investigate the effect of temperature and pore fluid pressure on the frictional properties of the simulated Pohang granodiorite gouge. The second group of experiments (Gr-150, E1G8-150, E2G7-150, E5G5-150, Ep-150) were carried out at σ_c = 110 MPa, P_f = 42 MPa, T = 150°C and epidote contents of 0–100 (0 12.5, 25, 50, and 100) vol.%, to explore the effect of epidote content on the frictional strength and stability of simulated granodiorite gouge. The third group of experiments (HM-150, 2CQ-150, 4CQ-150, EC-150) on 50:50 vol.% Gr:Ep were conducted at the in-situ temperature and pressure but with different gouge structures to define controls of epidote gouge micro-structure on frictional properties.

At the initiation of each experiment, the confining pressure and pore fluid pressure were applied by gas pump and hydraulic pump, respectively, to approximately two-thirds of the desired values. The temperature was then raised to the ultimate value at a rate of 5°C/min. The accuracies of the confining pressure and pore fluid pressure are ±0.5 and ±0.3 MPa, respectively, with deionized water adopted as the pore fluid. As the confining pressure in our experiments was applied by argon gas, the gas pressure increased with an increase in temperature. Therefore, after reaching the desired temperature, we adjusted the confining pressure and pore fluid pressure to the desired values. In each experiment, the sample was initially sheared at an axial displacement rate of 1.0 μm/s until approaching steady state friction. To evaluate the velocity dependence of friction, the axial displacement rates were incremented or decremented among 1.0, 0.2, and 0.04 μm/s, corresponding the along-fault shear velocities of 1.22, 0.244, and 0.0488 μm/s. The axial displacements at each incremented/decremented velocity were designed to be ~0.3 mm (~0.366 mm at the shear direction) at shear velocities of 1.22 and 0.244 μm/s, and 0.2 mm (~0.244 mm at the shear direction) at a shear velocity of 0.0488 μm/s. The axial load and displacement were recorded by external load cell and high-precision displacement sensor with a sampling frequency of 1 Hz. The temperature during the full experiment was monitored and controlled by a Yamatake-Honeywell DCP30 industrial controller with an accuracy of ±2°C.

2.3. Data Analysis

Due to the variation in gouge contact area with increasing shear displacement and a shear resistance from the copper jacket, the raw experimental data were corrected following the methods in He et al. (2006) and Verberne et al. (2010) and described in Text T2 in Supporting Information S1. The coefficient of friction was calculated by the ratio of final corrected shear stress (τ) to the effective normal stress (σ_{neff}; ignoring cohesion), expressed as,

$$\mu = \tau/\sigma_{neff} = \tau/(\sigma_n - P_f) \quad (1)$$

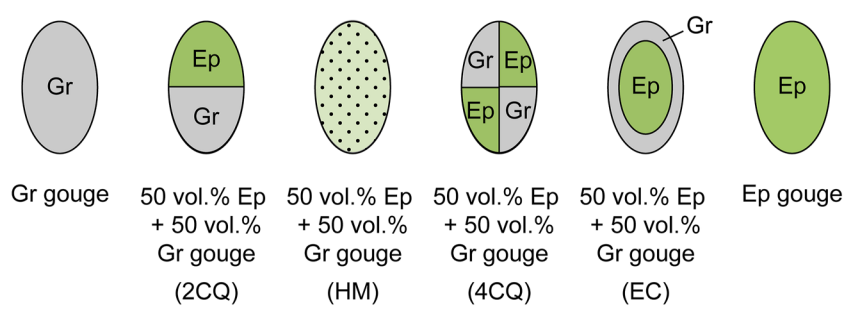

Figure 4. Schematic plot showing gouge structures as homogeneously mixed (HM), encapsulated (EC), and as halved- (2CQ) and then quartered- (4CQ) checkerboard.

Table 1
Details of the Twelve Shear Experiments

Experiment ID	Gouge composition	σ_c (MPa)	P_f (MPa)	T (°C)	l_f (mm)	V Dependence
Gr-100	Granodiorite	110	42	100	3.82	Vs
Gr-150	Granodiorite	110	42	150	2.98	Vs/Vw
Gr-150-63	Granodiorite	110	63	150	3.59	Vs/Vw
Gr-200	Granodiorite	110	42	200	3.27	Vs/Vw/Ss
Gr-250	Granodiorite	110	42	250	3.85	Vw/Ss
E1G8-150	12.5 vol.% epidote + 87.5 vol.% granodiorite (HM)	110	42	150	2.62	Vs/Vw
E2G7-150	25 vol.% epidote + 75 vol.% granodiorite (HM)	110	42	150	3.91	Vs/Vw
E5G5-150 (HM-150)	50 vol.% epidote + 50 vol.% granodiorite (HM)	110	42	150	3.84	Vw/Ss
2CQ-150	50 vol.% epidote + 50 vol.% granodiorite (2CQ)	110	42	150	3.86	Vs/Vw/Ss
4CQ-150	50 vol.% epidote + 50 vol.% granodiorite (4CQ)	110	42	150	3.89	Vw/Ss
EC-150	50 vol.% epidote + 50 vol.% granodiorite (EC)	110	42	150	3.86	Vw/Ss
Ep-150	Epidote	110	42	150	3.77	Vw/Ss

Note. The symbols σ_c, P_f, T, and l_f represent the applied confining pressure, pore fluid pressure, temperature and final shear displacement, respectively. The abbreviations Vs, Vw, and Ss indicate the observed behaviors as velocity-strengthening, velocity-weakening, and stick-slip, respectively. Gouge structures HM, 2CQ, 4CQ, and EC are shown in Figure 4.

where P_f is the applied pore fluid pressure.

The velocity dependence of friction was analyzed based on rate and state friction (RSF) theory (Dieterich, 1979; Marone, 1998; Ruina, 1983). Applying RSF theory to modeling fault slip defines the coefficient of friction μ as,

$$\mu = \mu_0 + aln\left(\frac{V}{V_0}\right) + bln\left(\frac{V_0\theta}{D_c}\right) \tag{2}$$

where μ is the coefficient of friction at the current shear velocity V, μ_0 is the steady state coefficient of friction at the reference shear velocity V_0 ($V > V_0$), a and b are dimensionless constants that describe the direct and evolutional effects from the change of the shear velocity, respectively, D_c is the critical shear displacement from a reference steady state toward a new steady state, and θ is a state variable associated with the average lifespan of grain/asperity contacts. The evolution of the state variable is described by the Dieterich law (or aging law) (Dieterich, 1979), expressed as,

$$\frac{d\theta}{dt} = 1 - \frac{V\theta}{D_c} \tag{3}$$

or the Ruina law (or slip law) (Ruina, 1983) with the expression of,

$$\frac{d\theta}{dt} = -\frac{V\theta}{D_c}\ln\left(\frac{V\theta}{D_c}\right) \tag{4}$$

An idealized rate and state friction response to an increase in shear velocity is shown in Figure 5. Frictional stability is partially determined by the parameter $(a - b)$ derived from Equations 2 and 3 at steady state friction ($d\theta/dt = 0$), expressed as,

$$a - b = \Delta\mu_{ss}/\Delta\ln(V) \tag{5}$$

where $\Delta\mu_{ss}$ is the difference in steady state coefficients of friction before then after a velocity step. Positive values of $(a - b)$ indicate that the coefficient of friction increases as shear velocity increases, that is, velocity-strengthening behavior, indicative of inherently stable and aseismic fault slip. In contrast, negative values $(a - b)$ indicate a decrease in friction with an increase in shear velocity, that is, velocity-weakening behavior, promoting unstable

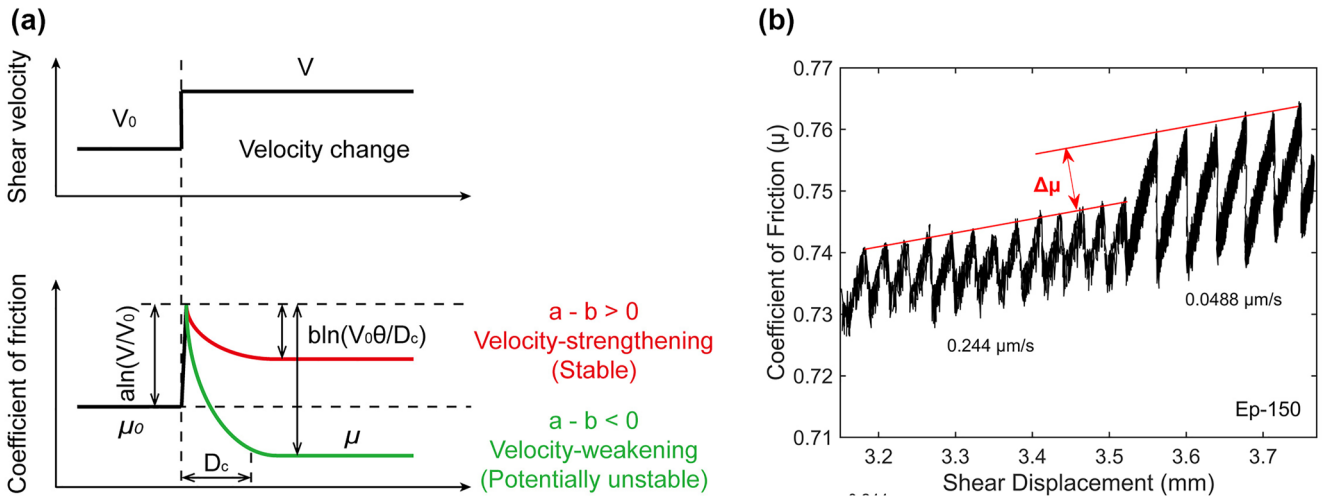

Figure 5. (a) Idealized rate and state friction response to an increase in shear velocity. (b) An example for determining the magnitude of $\Delta\mu$ during stick-slips.

and potentially seismic fault slip when the critical stiffness (K_{cr}) is also met. The critical stiffness of the fault is defined as,

$$K_{cr} = \frac{(b-a)\cdot\sigma_n}{D_c} \tag{6}$$

Fault instability also requires that the loading stiffness K is smaller than the critical stiffness K_{cr}, that is, $K \le K_{cr}$ (Gu et al., 1984). The stick-slip behavior is an unambiguous indicator of velocity-weakening response. For gouges with stick-slips, values of $(a-b)$ were estimated from the difference in peak coefficients of friction (Figure 5b), following Pluymakers et al. (2014).

2.4. Microstructural Methods

After the shear experiments, we carefully removed the corundum and tungsten carbide blocks with only the gouge-filled gabbro driving blocks wrapped by the copper jacket remaining. These were retained and dried at ~50°C for 48 hr to remove the moisture. The samples were then impregnated with epoxy resin in a vacuum chamber and placed in a temperature-controlled cabinet for ~24 hr until the epoxy had completely hardened. Thin sections were then cut along the axis of the cylindrical driving blocks and perpendicular to the fault plane. The thin sections were polished then gold coated and analyzed by a scanning electron microscopy (SEM).

3. Results

3.1. Pohang Granodiorite Gouge

The coefficient of friction for Pohang granodiorite powder exhibits initially rapid strain hardening followed by macroscopic yield at shear displacements of 1.0–1.5 mm. This is in turn followed by slight strain hardening response until the final shear displacements of 3–4 mm (Figure 6). The simulated granodiorite gouge shows stable sliding behavior at $T \le 150$°C (Figures 6a–6c), while stick-slips were observed at a shear velocity of 0.0488 μm/s at $T = 200$°C (Figure 6d) and shear velocities of 1.22 and 0.244 μm/s at $T = 250$°C (Figure 6e). We compare the coefficients of friction of each experiment at a standard ~2.5 mm shear displacement and 1.22 μm/s shear velocity. The coefficients of friction of the Pohang granodiorite powder at different temperatures ($T = 100$–250°C) and pore fluid pressures ($P_f = 42$–63 MPa) are all close to 0.71 (Table 2 and Figure 7a), indicating that the friction coefficient is insensitive to both temperature and pore fluid pressure over the range studied.

The simulated Pohang granodiorite gouge (Figure 7b) undergoes a transition from velocity-strengthening behavior ($a - b = 0.0016$ to 0.0025) at $T = 100$°C, to velocity-neutral behavior ($a - b = -0.0003$ to 0.0011) at

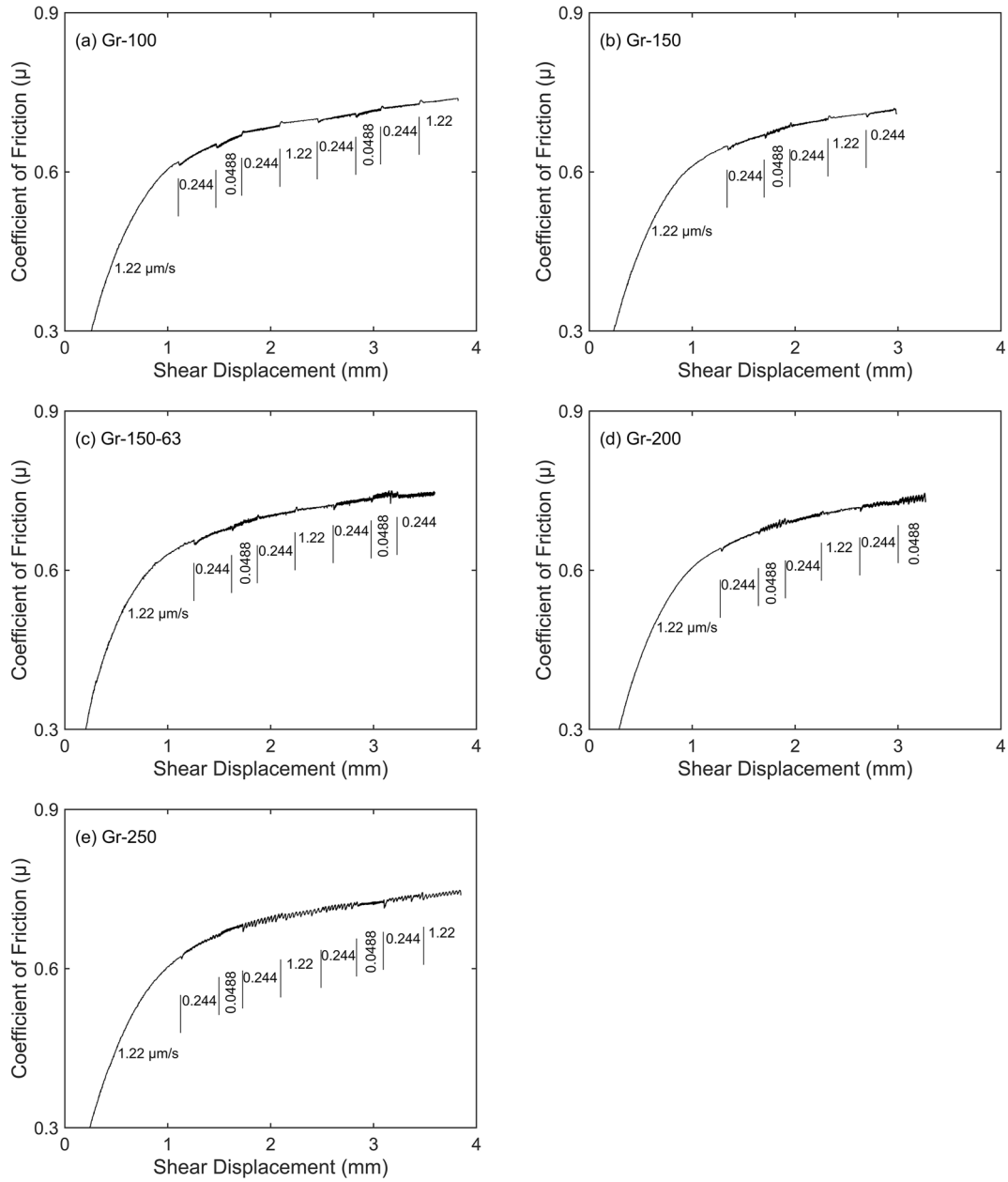

Figure 6. Friction-displacement curves for the simulated Pohang granodiorite gouge at conditions: (a) $T = 100$°C, $P_f = 42$ MPa, (b) $T = 150$°C, $P_f = 42$ MPa, (c) $T = 150$°C, $P_f = 63$ MPa, (d) $T = 200$°C, $P_f = 42$ MPa, and (e) $T = 250$°C, $P_f = 42$ MPa.

$T = 150$°C, then velocity-weakening behavior at $T = 200$°C ($a - b = -0.0044$ to 0.0006) and $T = 250$°C ($a - b = -0.0033$ to -0.0014) – indicating a higher potential for fault instability at higher temperatures. Elevating the pore fluid pressure at $T = 150$°C also destabilizes the simulated fault gouge ($a - b = -0.0003$ to 0.0011 at $P_f = 42$ MPa, and $a - b = -0.0016$ to 0.0009 at $P_f = 63$ MPa), implying that the effective normal stress also exerts a control on fault stability.

3.2. Epidote-Granodiorite Mixed Gouges for Different Epidote Proportions

To examine the effect of epidote proportion on the frictional and stability properties of simulated granodiorite gouge, we varied the epidote contents to 0, 12.5, 25, 50, and 100 vol.%. The epidote-granodiorite gouges were

Table 2
Results of the Twelve Shear Experiments

Experiment ID	μ_{ss}	$a-b$ values at (μm/s)			
		0.244–0.0488	0.0488–0.244	0.244–1.22	1.22–0.244
Gr-100	0.700	0.0016 ± 0.0011	0.0025 ± 0.0009	0.0020 ± 0.0008	0.0020
Gr-150	0.706	−0.0003	0.0002	0.0011	0.0003
Gr-150-63	0.720	−0.0010 ± 0.0007	−0.0016 ± 0.0016	0.0009	−0.0012
Gr-200	0.715	−0.0034 ± 0.0013	−0.0044	0.0006	−0.0017
Gr-250	0.710	−0.0027 ± 0.0001	−0.0033 ± 0.0007	−0.0017 ± 0.0003	−0.0014
E1G8-150	0.702	−0.0008	0	0.0007	–
E2G7-150	0.704	−0.0023 ± 0.0009	−0.0012 ± 0.0012	−0.0002 ± 0.0008	−0.0014
E5G5-150 (HM-150)	0.718	−0.0046 ± 0.0028	−0.0040 ± 0.0029	−0.0006 ± 0.0006	−0.0017
2CQ-150	0.715	−0.0023 ± 0.0017	−0.0033 ± 0.0017	−0.0002 ± 0.0005	−0.0008
4CQ-150	0.719	−0.0045 ± 0.0008	−0.0051 ± 0.0007	−0.0010 ± 0.0007	−0.0017
EC-150	0.721	−0.0057 ± 0.0020	−0.0042 ± 0.0016	−0.0008 ± 0.0004	−0.0024
Ep-150	0.730	−0.0062 ± 0.0003	−0.0053	−0.0057	−0.0039

Note. The frictional stability parameter ($a-b$) values were the average values from the same velocity steps in each test with the errors calculated from the standard deviations. Values of ($a-b$) in each shear velocity are also shown in Table S1 in Supporting Information S1. The first velocity step (1.22–0.244 μm/s) was excluded in the calculation. μ_{ss} = coefficient of friction determined at ~2.5 mm shear displacement and a sliding velocity of 1.22 μm/s.

HM and evaluated at the identical condition of σ_c = 100 MPa, P_f = 42 MPa, and T = 150°C. The friction-displacement curves for the mixed gouges are shown in Figure 8. The mixed gouges exhibited slight strain-hardening response after the first 1–2 mm shear displacement. When the epidote content is below 25 vol.%, the mixed gouges show stable sliding. In contrast, stick-slips were observed at the second velocity of 0.0488 μm/s for the 50:50 epidote:granodiorite mixed gouge and at 0.244 and 0.0488 μm/s for the pure epidote gouge.

The coefficient of friction μ and frictional stability ($a-b$) for the HM gouges are summarized in Table 2 and Figure 9. The pure epidote gouge is frictionally strong and show a friction coefficient of ~0.73. With an increase in epidote content for the mixed gouges, the variation in coefficient of friction is negligible (increasing from ~0.70 to ~0.73), intermediate between those for pure epidote ($\mu \sim 0.730$) and the simulated Pohang granodiorite ($\mu \sim 0.706$) gouge. The mixed gouges (Figure 9b) become increasingly unstable with increasing epidote content. This is indexed by ($a-b$) decreasing with increased epidote content progressing from 0 vol.% epidote ($a-b$ = −0.0003 to 0.0011), 12.5 vol.% epidote ($a-b$ = −0.0008 to 0.0007), 25 vol.% epidote ($a-b$ = −0.0023 to −0.0002), 50 vol.% epidote ($a-b$ = −0.0046 to −0.0006), to 100 vol.% epidote ($a-b$ = −0.0062 to −0.0039).

3.3. Epidote-Granodiorite Mixed Gouges of Different Structures

To further explore the effect of various gouge structures on the frictional response, we varied the geometries for the 50:50 epidote:granodiorite mixed gouge for the single set of environmental conditions of σ_c = 110 MPa, P_f = 42 MPa, and T = 150°C. The structures are for HM, then EC, 2CQ, and 4CQ samples in order of decreasing patch size. The friction-displacement curves are shown in Figures 8c and 10. For each gouge structure, the simulated gouge is strongly strain hardening over the initial 1–2 mm of shear displacement, followed by a transition to mildly strain hardening at the final shear displacement of ~4 mm. Stick-slips were observed at a shear velocity of 0.0488 μm/s for all four gouge structures.

We compare the frictional properties of the 50:50 epidote:granodiorite mixed gouge in different structures against those for pure epidote and the simulated Pohang granodiorite gouge (Table 2 and Figure 11). The coefficients of friction for the 50:50 gouges all approach ~0.72, independent of configuration. This is slightly higher than that of the simulated Pohang granodiorite gouge ($\mu \sim 0.706$) and slightly lower than that of the pure epidote ($\mu \sim$ 0.73; Figure 11a). This indicates that the gouge structure has negligible impact on the overall frictional strength

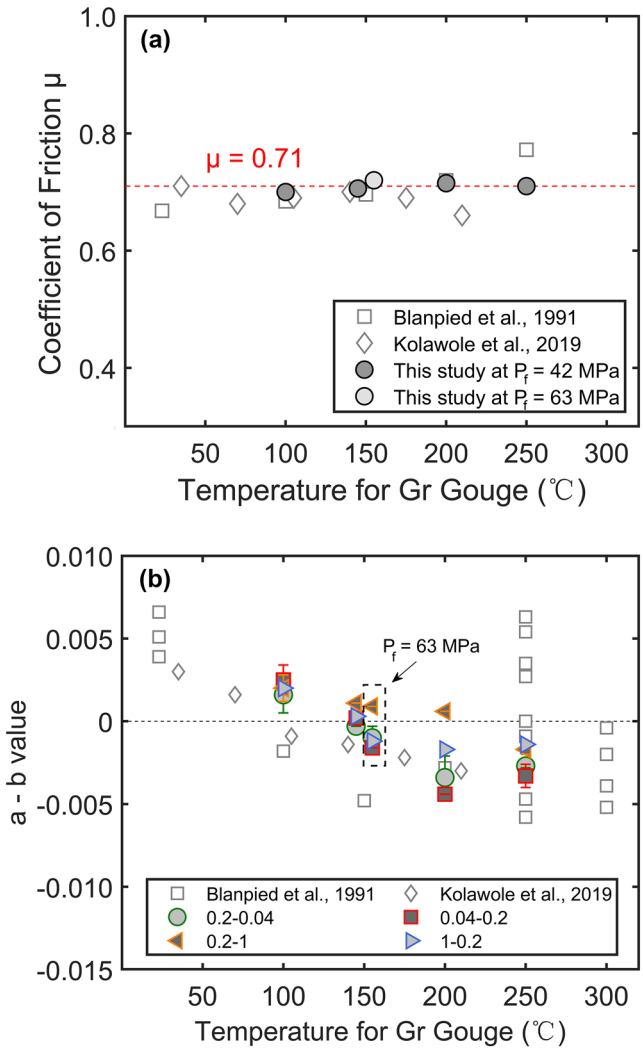

Figure 7. (a) Coefficient of friction μ and (b) velocity dependence ($a - b$) for the simulated Pohang granodiorite (Gr) gouge at different temperatures and pore fluid pressures and other reported granitic gouges at different temperatures. The hollow squares and diamonds represent the results from Blanpied et al. (1991) and Kolawole et al. (2019), respectively (Table S2 in Supporting Information S1). The solid circles in (a) and colorful symbols in (b) represent the results of this study. The red dashed line in (a) indicates $\mu = 0.71$ and the legend in (b) denotes the axial displacement rate.

which is bracketed by these pure mixes. The different geometric mixtures all indicate apparent velocity-weakening response (Figure 11b), contrary to the velocity-neutral behavior of the simulated Pohang granodiorite gouge. This confirms the destabilizing effect of epidote in a matrix of granodiorite, similar to the trend for variable proportions of epidote (Figure 9). The encapsulated gouge EC ($a - b = -0.0057$ to -0.0008) shows similar values of ($a - b$) with the quartered-checkerboard 4CQ ($a - b = -0.0051$ to -0.0010), but lower than that at the homogeneously mixed gouge HM ($a - b = -0.0046$ to -0.0006) and 2CQ ($a - b = -0.0033$ to -0.0002; Table 2 and Figure 11). This suggests that gouge structure exerts an impact on the frictional stability of the mixes. In particular, the homogeneous and encapsulated structures HM and EC show lower values of ($a - b$) at the lowest shear velocities (S0.244-0.0488 in Table S1 in Supporting Information S1, $a - b = -0.0073$ for HM-150 and -0.0076 for EC-150) than the pure epidote gouge ($a - b = -0.0059$). In addition, the values of ($a - b$) for all four gouge structures also show a strong dependence on the shear velocities (Figure 11b). The ($a - b$) values at shear velocities of 0.244–1.22 μm/s and 1.22–0.244 μm/s are higher than those obtained at shear velocities of 0.244–0.0488 μm/s and 0.0488–0.244 μm/s. However, the trend is not evident for the pure epidote or the simulated Pohang granodiorite gouges.

3.4. Microstructural Observations

Following the methods described in Section 2.4, the microstructures of the deformed gouges in the three groups of experiments are illustrated in Figures 12–14, respectively. The terminology of Logan et al. (1992) is employed to describe the gouge shear characteristics. R1 (Riedel) fractures are generally abundant in the deformed gouge zones and they are at relatively high angles to the gouge-forcing block interface and widely spaced.

For Pohang granodiorite, the deformed gouges at different temperatures and pore fluid pressures are shown in Figure 12, with minor R1 fractures observed for $T = 100$°C and $P_f = 42$ MPa (Figure 12a) where the gouge exhibits velocity-strengthening behavior. At higher temperatures and pore fluid pressures, a denser array of R1 fractures formed across the gouge zone and these gouges all show velocity-weakening behaviors (Figures 12b–12d), indicating a higher correlation between the R1 fractures with the temperature and pore fluid pressure for the simulated granodiorite gouge. For epidote-granodiorite HM gouges at different epidote proportions (Figures 13a–13c), all gouges exhibit dense R1 fractures and velocity-weakening responses. The epidote particles in the R1 shear zones are subject to stronger comminution than those in the flanking zones, resulting in localized shear zones around the R1 fracture zones.

For deformed epidote-granodiorite mixed gouges of different structures, we select the upper and lower section of the elliptical sample on a single side of the shear zone of the halved-checkerboard sample 2CQ-150, lower right section of the quartered-checkerboard sample 4CQ-150, and the central section of the EC sample EC-150 to illustrate the microstructural evolution at 150°C, as shown in Figure 14. From Figure 4, the upper and lower section of the ellipse of sample 2CQ-150 correspond to the epidote and granodiorite gouges, respectively. The lower right section of sample 4CQ-150 is granodiorite gouge and the central section of the sample EC-150 is mainly epidote gouge. In sample 2CQ-150 (Figures 14a and 14b), large R1 fractures are observed in the upper section filled by epidote gouge, while fewer R1 fractures are visible in the lower section filled by the simulated Pohang granodiorite gouge. Similarly, minor R1 fractures are also apparent in sample 4CQ-150 (Figure 14c), but many fewer than in the pure simulated granodiorite gouge under the same testing conditions ($\sigma_c = 110$ MPa,

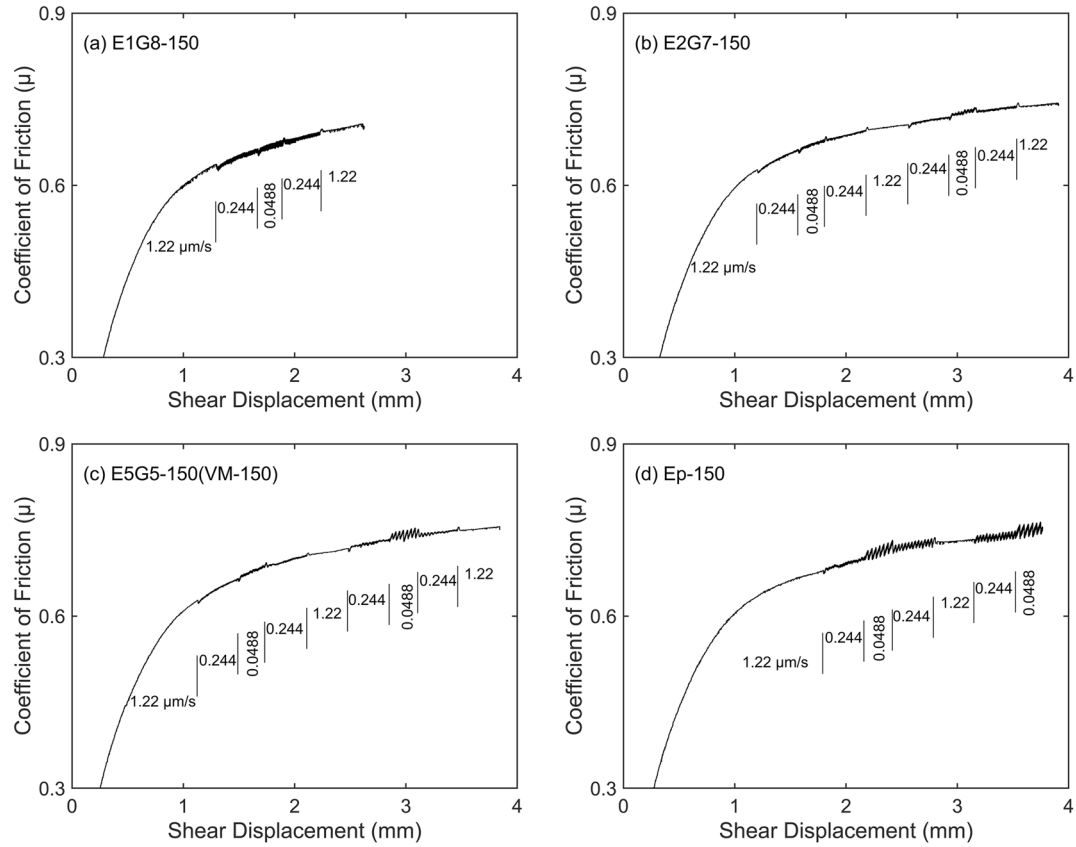

Figure 8. Friction-displacement curves for different gouges at $\sigma_c = 110$ MPa, $T = 150$°C, and $P_f = 42$ MPa: (a) 12.5:87.5 epidote:granodiorite gouge, (b) 25:75 epidote:granodiorite gouge, (c) 50:50 epidote:granodiorite gouge, and (d) pure epidote gouge.

$P_f = 42$ MPa, $T = 150$°C; Figure 12b). Additionally, large R1 fractures are observed in the central section of the EC sample EC-150 (Figure 14d), similar to the upper section of halved-checkerboard sample 2CQ-150. In addition, we noted no anomalous features at the Gr-Ep boundaries for samples 2CQ-150 and 4CQ-150 (Figure S3 in Supporting Information S1).

4. Discussion

4.1. Comparison With Literature Data

The dependence of the friction coefficient of granitic gouges at temperatures 20–300°C from previous studies is significantly different from that for our powdered Pohang granodiorite. We compare our results with the friction coefficients of Westerly granite and other simulated granitic gouges at hydrothermal conditions (Blanpied et al., 1991; Kolawole et al., 2019; Figure 7a). The coefficient of friction of Westerly granite gouge at $\sigma_{neff} = 400$ MPa and $P_f = 100$ MPa increases from ~0.67 to 0.77 at temperatures 23–250°C (Blanpied et al., 1991). Troy granite (one granite defined in Kolawole et al. (2019)) gouge under hydrothermal conditions exhibits friction coefficients of ~0.70 at 35–175°C, but decreases (~0.66) at 210°C (Kolawole et al., 2019). The stability transition temperatures for the reported granitic gouges are also variable and depend on the testing conditions. For example, the transition from velocity-strengthening to velocity-weakening behavior of Westerly granite gouge occurs at $T = 100$°C under hydrothermal conditions (Blanpied et al., 1991; Figure 7b). Similarly, the Troy granite and Osage microgranite (defined in Kolawole et al. (2019)) gouges begin to show velocity-weakening behavior at $T = 105$°C and 175°C, respectively (Kolawole et al., 2019; Figure 7b). The dependences of fault gouge stability on effective stresses were also reported in Niemeijer and Vissers (2014) on phyllosilicate-rich gouges obtained from the Alhama de Murcia Fault and Sawai et al. (2016) on blueschist gouge.

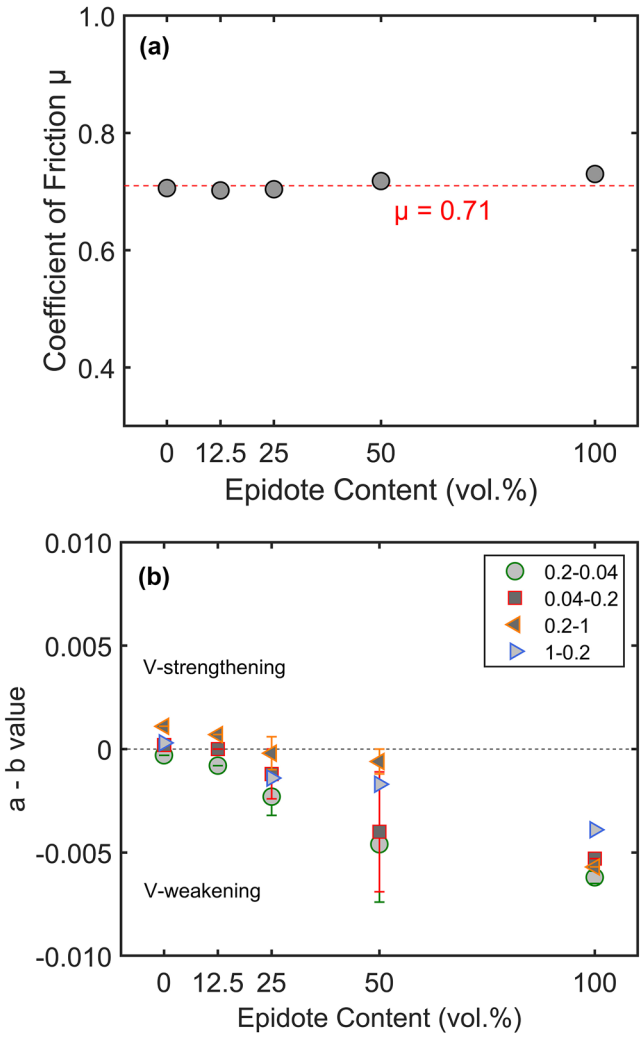

Figure 9. (a) Coefficient of friction μ and (b) velocity dependence $(a - b)$ for epidote-granodiorite mixed gouges at different epidote proportions at $\sigma_c = 110$ MPa, $P_f = 42$ MPa, and $T = 150$°C. The red dashed line in (a) indicates $\mu = 0.71$ and the legend in (b) denotes the axial displacement rate.

The coefficient of friction of epidote gouge (~0.73) is consistent with the reported friction coefficient of ~0.72 of epidote gouge recovered from veins and tested under hydrothermal conditions ($\sigma_c = 165$ MPa, $P_f = 60$ MPa, and $T = 140$°C; Kolawole et al., 2019; Table S2 in Supporting Information S1). However, this is higher than the coefficient of friction of ~0.63 of epidotite gouge (69% epidote, 20% amphibole, and 11% sphene) at a normal stress of 10 MPa and at room temperature (Fagereng & Ikari, 2020). Our results for the frictional stability of epidote gouge are in accordance with the results of previous studies (Fagereng & Ikari, 2020; Kolawole et al., 2019) that the epidote-rich gouges tend to exhibit velocity-weakening behavior under both hydrothermal conditions and dry and at room temperature.

4.2. The Dependence of Granitoid Fault Stability on Temperature and Pressure

The magnitudes of temperature and pore fluid pressure are both important factors affecting fault stability with both factors potentially controlling the effective viscosity of gouge asperity contacts (Blanpied et al., 1995; Lockner et al., 1986). The simulated Pohang granodiorite gouge in this study undergoes a transition from velocity-strengthening behavior at 100°C, to velocity-neutral behavior at 150°C, then velocity-weakening behavior at 200–250°C (Figure 7b). Many simulated granitoid gouges (e.g., Blanpied et al., 1991; Kolawole et al., 2019; Mitchell et al., 2016) also exhibit a similar transition from velocity-strengthening to velocity-weakening with an increase in temperature over the temperature range 0–250°C. The difference between these simulated granitoid gouges is the different threshold/critical temperature for this transition with this critical temperature also depending on the gouge composition. A widely accepted theory to interpret the fault weakening mechanism at elevated temperatures is a microphysical model advanced in Niemeijer and Spiers (2007), den Hartog et al. (2012), and den Hartog & Spiers (2013). This microphysical model attributes the changes in velocity dependence of frictional stability to the styles of deformation of gouge aggregates. This invokes processes of shear-induced gouge intergranular dilation and porosity reduction (compaction) by pressure solution as key controls on fault frictional stability. High temperatures accelerate the rate of pressure solution and reduce porosity and thereby densify the gouge structure obtained at steady state of friction. Under this condition, increasing the shear velocity promotes gouge dilation that then dominates over any compaction and leads to the porosity increase at higher shear velocities. This produces a lower frictional strength in response to an incremented velocity step and observed velocity-weakening behavior.

For activities involving massive fluid injection, elevated pore fluid pressures typically reduce the effective stress and may promote fault reactivation (Ellsworth, 2013; Guglielmi et al., 2015). The first injection operation in well PX-2 at the Pohang site resulted in a wellhead pressure ~89 MPa and a bottom-hole pressure of 132 MPa at a depth of 4,368 m (Park et al., 2020). The pore fluid pressures are limited in our apparatus so we elevate the pore fluid pressure to only 63 MPa (1.5 × hydrostatic pressure). Our results (Figure 7b) indicate that the stability of the simulated Pohang granodiorite gouge still depends slightly on the magnitude of the effective normal stress (or pore fluid pressure). Similar results noting the dependence of the rate-weakening parameter $(a - b)$ to effective stress are also reported in several experimental studies (e.g., den Hartog & Spiers, 2013; Niemeijer & Vissers, 2014; Sawai et al., 2016). den Hartog & Spiers (2013) reported that decreasing the effective normal stress of illite-rich Rochester shale gouge (quartz-phyllosilicate mixtures) favors fault stability. And similar results are also documented by Niemeijer and Vissers (2014) on phyllosilicate-rich gouges from the Alhama de Murcia fault, Spain. However, our results are counter to these observations but consistent with results for blueschist gouges (mainly glaucophane and lawsonite) at higher temperatures (>200°C: Sawai et al., 2016). In rationalizing this

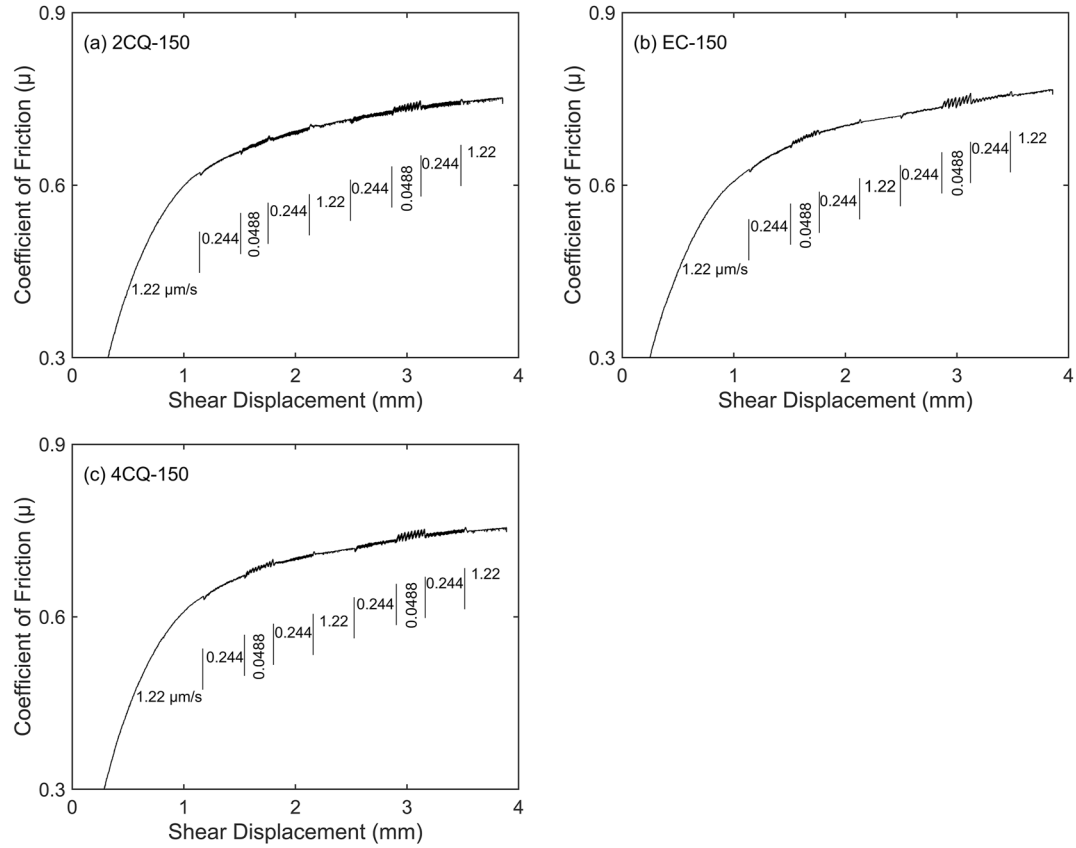

Figure 10. Friction-displacement curves for 50:50 epidote:granodiorite mixed gouge with different structures at $\sigma_c = 110$ MPa, $T = 150$°C, and $P_f = 42$ MPa: (a) halved-checkerboard (2CQ), (b) encapsulated (EC), and (c) quartered-checkerboard (4CQ).

discrepancy between various measurements, we speculate that our results are also affected by the evolution of fault permeability. From Faulkner et al. (2018), the rate-weakening parameter $(a - b)$ can switch from positive to negative when the pore fluid pressure is disequilibrated – this phenomenon highlights the role of higher pore fluid pressures in promoting the fault instability. In addition, Mitchell et al. (2016) showed an absence of dependence of $(a - b)$ on effective normal stress for dry Westerly granite gouge. This also supports the suggestion that the effects of water content and permeability evolution are important in assessing fault stability.

4.3. Implications for Injection-Induced Seismicity

The potential precipitation of epidote highlights the importance of the interactions between the hot fluids and natural fracture/fault surfaces (Franz & Liebscher, 2004). The circulation of hot fluids requires that the fracture/fault zones are sufficiently permeable. Thus, an important question remains as to whether fault structures favor the access and then precipitation of metamorphic epidote and what controls such processes. We briefly discuss the relationship between fault permeability structure and epidote precipitation in Text T3 in Supporting Information S1. Apparently, localized conduit, distributed conduit, and combined conduit-barrier structures all contain permeable zones for the circulation of hot fluids rendering the localized barrier structure as an exception (Figures S4 and S5 in Supporting Information S1; Caine et al., 1996; Choi et al., 2016). Our observations of epidote-granodiorite mixed gouges of different structures (Figure 11; HM-150, EC-150, 2CQ-150, and 4CQ-150) show comparable velocity-weakening behavior to that of the pure epidote gouge but stronger velocity-weakening behavior to the simulated granodiorite gouge. Apparent from the microstructures are that more localized fractures and shears develop within the epidote relative to the simulated granodiorite gouge (Figures 12–14). These results also indicate that the local precipitation of epidote in either fault damage zones or fault core zones could influence the fault frictional stability.

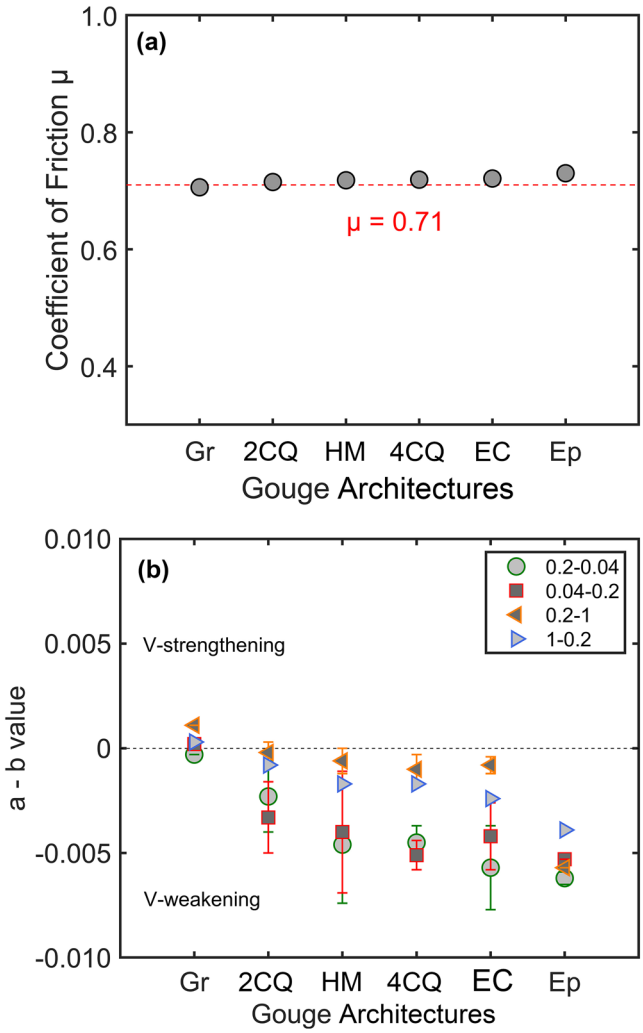

Figure 11. (a) Coefficient of friction μ and (b) velocity dependence ($a - b$) for 50:50 epidote:granodiorite mixed gouge at different structures. The red dashed line in (a) indicates $\mu = 0.71$ and the legend in (b) denotes the axial displacement rate.

Our results have implications in understanding injection-induced earthquakes related to EGS and wastewater injection (Kolawole et al., 2019; Olasolo et al., 2016), as well as other related activities. The temperature (100–200°C) for transition from rate-strengthening to rate-weakening behavior of simulated granitoid gouges (Figure 7) indicates that granitoid faults are potentially unstable and may nucleate earthquakes at shallow depths. Both magnitude of pore fluid pressure and the temperature are also important controls on granitoid fault stability. These observations can help understand the clusters of injection-induced earthquakes in granitoid reservoirs.

The transition temperature (100–125°C) promoting the occurrence of velocity-weakening behavior of epidote gouges is similar to, or even lower than, that currently reported for granitoid faults (An et al., 2021; Blanpied et al., 1991, 1995; Kolawole et al., 2019; Mitchell et al., 2016). This suggests that the enrichment of epidote in granitoid fault zones may be another important control on granitoid fault stability under hydrothermal conditions. The in-situ temperature of the Pohang geothermal reservoir at 4.2 km is ~150°C and the general temperature range for enhanced geothermal systems is 150–250°C (Olasolo et al., 2016). Native fractures in the Pohang granodiorite (Figure 2) indeed show epidotization – confirming the potential for epidote precipitation in shallow geothermal reservoirs. Although the exact abundance and distribution of the epidote in the fault system at the Pohang geothermal site is uncertain, its presence in adjacent fractures and broadly within similar environments worldwide points to its potential significance with regard to triggered seismicity and reservoir performance. Additionally, the presence of low-grade metamorphic minerals is widely reported at many geoengineering sites, including at Pohang in South Korea, the Gonghe Basin in China and associated with deep disposal in Oklahoma in the United States (Cheng et al., 2021; Kolawole et al., 2019; Lee, Yeo, et al., 2019; Zhang et al., 2020). Thus, such metamorphic reaction products (epidote) potentially exert important controls on fault stability and in thereby increasing the anthropogenic seismic hazard.

5. Conclusions

We systematically explore the frictional strength and stability of a spectrum of gouge mixtures with end members of pure epidote and pure granodiorite as representative of faults derived from reservoir rocks. Experiments are completed at conditions typical of geothermal reservoirs to probe mechanisms and impacts of low-grade metamorphism on the frictional properties of faults in granitoids. In particular, we examine both homogeneous and structured mixtures to probe the influence of epidote distribution and patch size on imparted stability. We derive the following conclusions:

1. The frictional strengths of simulated Pohang granodiorite gouge at different temperatures and pressures are high (μ all approaching 0.71). At in-situ pore fluid pressure typifying the Pohang geothermal reservoir, the simulated granodiorite gouge undergoes a transition from velocity-strengthening behavior at 100°C, to velocity-neutral behavior at 150°C and finally velocity-weakening behavior at 200–250°C. In particular, decreasing the effective normal stress (or elevating the pore fluid pressure) can further destabilize the simulated Pohang granodiorite gouge, indicating that injecting fluids into faults may render them potentially unstable at shallow depths.
2. The pure epidote gouge shows a similar frictional strength ($\mu \sim 0.73$) to the simulated granodiorite gouge but exhibits a stronger and earlier onset of velocity-weakening behavior at hydrothermal conditions.
3. For HM epidote/granodiorite gouges with 12.5%, 25%, and 50% epidote, increasing the proportion of epidote maintains the high frictional strengths (μ of 0.70–0.72) but increases the velocity-weakening response. This

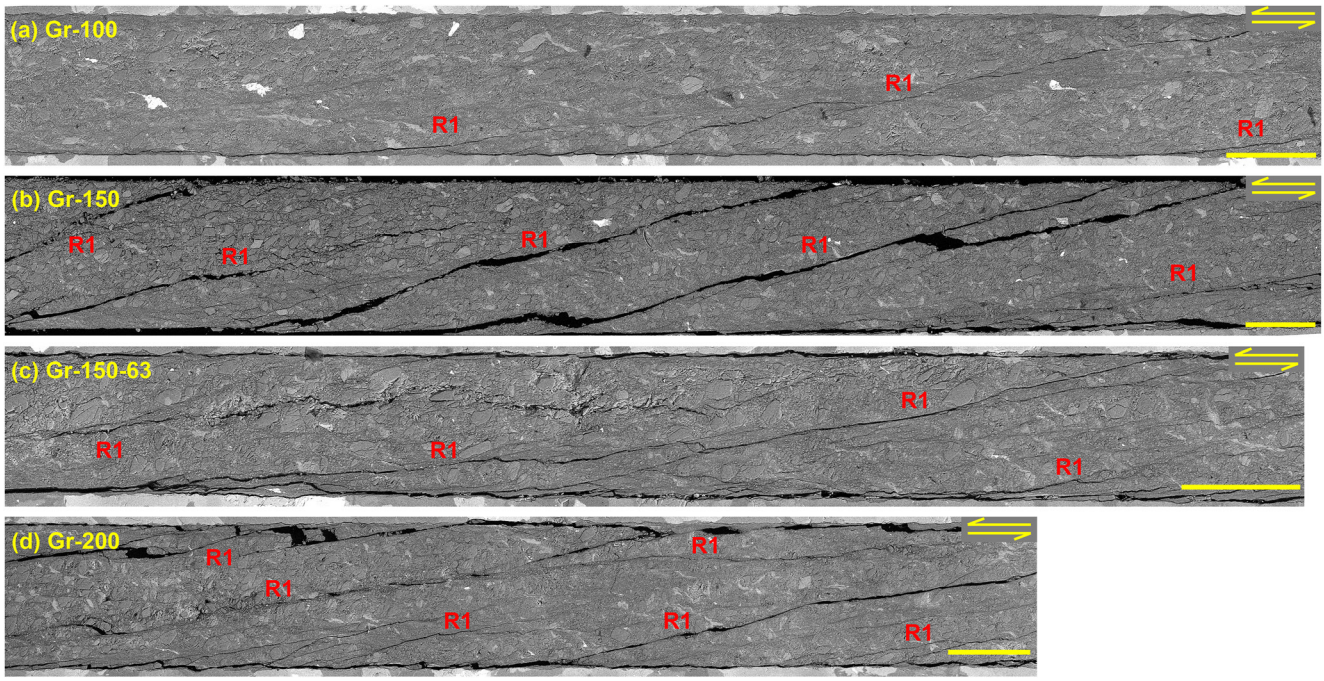

Figure 12. Microstructures (backscattered electron images) of the deformed simulated Pohang granodiorite gouges along the shear direction: (a) Gr-100, (b) Gr-150, (c) Gr-150-63, and (d) Gr-200. Only the deformed gouge in (a) exhibits the velocity-strengthening behavior and others all show velocity-weakening behaviors. Scale bars, 500 μm.

confirms the potential contribution of naturally present or fluid-circulation-deposited metamorphic epidote to seismic rupture.

4. The influence of epidote patch dimension is explored using a 50:50 mix of epidote:granodiorite with varied geometries and patch sizes. These structures include HM, the EC, 2CQ, and 4CQ, in order of decreasing patch size. All gouge structures result in velocity-weakening response similar to that for pure epidote gouge, largely independent of patch geometry. This velocity-weakening response is only slightly stronger than for homogeneously mixed gouge at 25% epidote – implying that the proportion of patch coverage is important but thickness is not. Thus, a thin but continuous layer of epidote, representative of a small volume percentage of

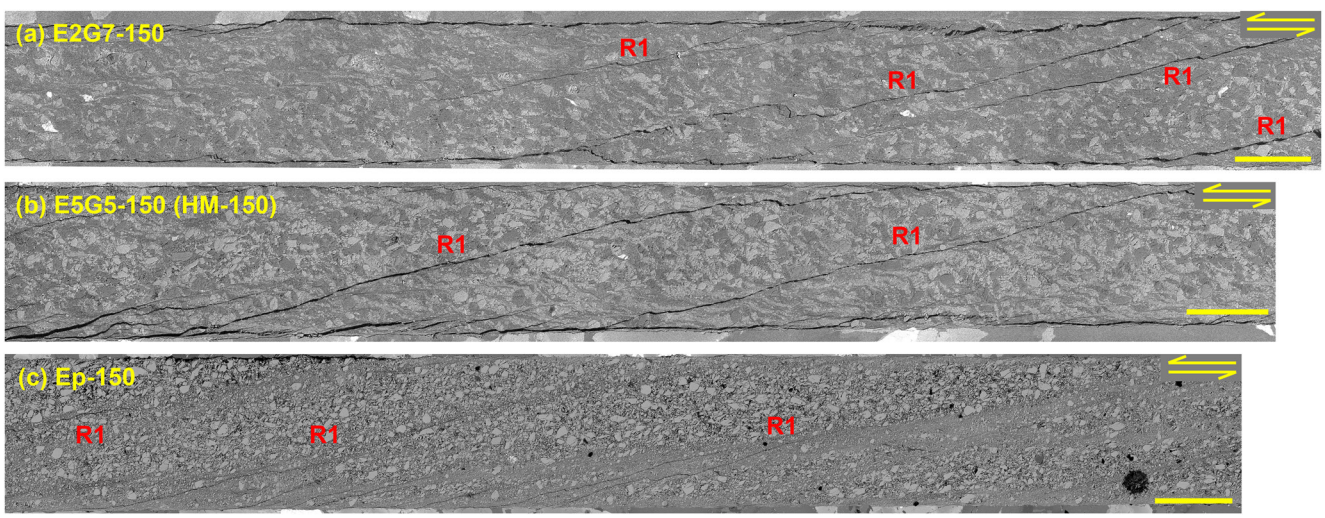

Figure 13. Microstructures (backscattered electron images) of the granodiorite-epidote mixed and pure epidote gouges along the shear direction: (a) E2G7-150, (b) E5G5-150 (HM-150), and (c) Ep-150. All deformed gouges show velocity-weakening responses. Scale bars, 500 μm.

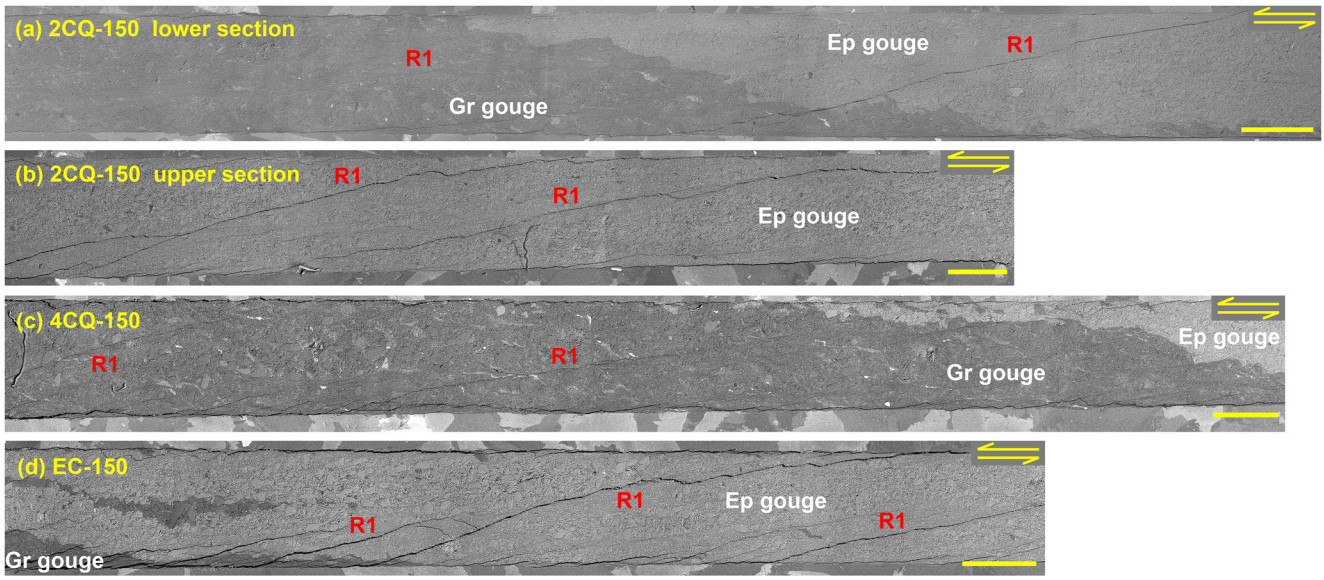

Figure 14. Microstructures (backscattered electron images) of the deformed granodiorite-epidote mixed gouges at different structures along the shear direction: (a) the lower section of 2CQ-150, (b) the upper section of 2CQ-150, (c) 4CQ-150, and (d) EC-150. All deformed gouges exhibit velocity-weakening behaviors. Scale bars, 500 μm.

epidote versus granodiorite, could likely impart the same velocity-weakening response. This supports the idea that small volumes of epidote deposited on fault plane fractures can support the seismic reactivation of faults.

5. High permeability zones are a necessary feature for the accumulation of hydrothermally-introduced metamorphic products (epidote) resulting from fluid-rock interactions. Considering the frictional and stability properties of epidote at conditions typical of shallow depths, the presence of low-grade metamorphism exerts an important control on fault stability in granitoids with relevance as a marker mineral for susceptibility to injection-induced seismicity.

Data Availability Statement

The friction data in this work can be found at https://doi.org/10.5061/dryad.7d7wm37vz.

Acknowledgments

This research is funded by the National Natural Science Foundation of China (41772286, 42077247, 42107163), the China Postdoctoral Science Foundation (2021M692448), and the Fundamental Research Funds for the Central Universities. The recovery of rock core from the Pohang EGS site was initially sponsored by a grant (No. 20123010110010) from the New and Renewable Energy Program of the Korea Institute of Energy Technology Evaluation and Planning, and funded by the Ministry of Trade, Industry and Energy of the Korean Government. XRD and microstructural characterization were conducted on natural granodiorite fractures recovered from Pohang Geothermal reservoir. We appreciate the assistance of Jianye Chen, Wenming Yao, Xi Ma, Yang Liu, Huiru Lei, and Wei Feng in conducting the experiments. We thank the helpful reviews from Diane Moore and an anonymous reviewer.

References

An, M., Zhang, F., Min, K.-B., Elsworth, D., Marone, C., & He, C. (2021). The potential for low-grade metamorphism to facilitate fault stability in a geothermal reservoir. *Geophysical Research Letters*, *48*(11), e2021GL093552. https://doi.org/10.1029/2021GL093552

Atkinson, G. M., Eaton, D. W., & Igonin, N. (2020). Developments in understanding seismicity triggered by hydraulic fracturing. *Nature Reviews Earth & Environment*, *1*(5), 264–277. https://doi.org/10.1038/s43017-020-0049-7

Bird, D. K., & Spieler, A. R. (2004). Epidote in geothermal systems. *Reviews in Mineralogy and Geochemistry*, *56*, 235–300. https://doi.org/10.2138/gsrmg.56.1.235

Blanpied, M. L., Lockner, D. A., & Byerlee, J. D. (1991). Fault stability inferred from granite sliding experiments at hydrothermal conditions. *Geophysical Research Letters*, *18*(4), 609–612. https://doi.org/10.1029/91GL00469

Blanpied, M. L., Lockner, D. A., & Byerlee, J. D. (1995). Frictional slip of granite at hydrothermal conditions. *Journal of Geophysical Research: Solid Earth*, *100*(B7), 13045–13064. https://doi.org/10.1029/95JB00862

Caine, J. S., Evans, J. P., & Forster, C. B. (1996). Fault zone architecture and permeability structure. *Geology*, *24*(11), 1025–1028. https://doi.org/10.1130/0091-7613(1996)024<1025:fzaaps>2.3.co;2

Caruso, L. J., Bird, D. K., Cho, M., & Liou, J. G. (1988). Epidote-bearing veins in the state 2-14 drill hole: Implications for hydrothermal fluid composition. *Journal of Geophysical Research: Solid Earth*, *93*(B11), 13123–13133. https://doi.org/10.1029/JB093iB11p13123

Cheng, Y., Zhang, Y., Yu, Z., & Hu, Z. (2021). Investigation on reservoir stimulation characteristics in hot dry rock geothermal formations of China during hydraulic fracturing. *Rock Mechanics and Rock Engineering*, *54*, 3817–3845. https://doi.org/10.1007/s00603-021-02506-y

Choi, J.-H., Edwards, P., Ko, K., & Kim, Y.-S. (2016). Definition and classification of fault damage zones: A review and a new methodological approach. *Earth-Science Reviews*, *152*, 70–87. https://doi.org/10.1016/j.earscirev.2015.11.006

den Hartog, S. A. M., Peach, C. J., Winterde , D. A. M., Spiers, C. J., & Shimamoto, T. (2012). Frictional properties of megathrust fault gouges at low sliding velocities: New data on effects of normal stress and temperature. *Journal of Structural Geology*, *38*, 156–171.

den Hartog, S. A. M., & Spiers, C. J. (2013). Influence of subduction zone conditions and gouge composition on frictional slip stability of megathrust faults. *Tectonophysics*, *600*, 75–90.

Dieterich, J. H. (1979). Modeling of rock friction: 1. Experimental results and constitutive equations. *Journal of Geophysical Research*, *84*(B5), 2161. https://doi.org/10.1029/JB084iB05p02161

Ellsworth, W. L. (2013). Injection-induced earthquakes. *Science*, *341*(6142), 1225942. https://doi.org/10.1126/science.1225942

Ellsworth, W. L., Giardini, D., Townend, J., Ge, S., & Shimamoto, T. (2019). Triggering of the Pohang, Korea, earthquake (Mw 5.5) by enhanced geothermal system stimulation. *Seismological Research Letters*. https://doi.org/10.1785/0220190102

Elsworth, D., Spiers, C. J., & Niemeijer, A. R. (2016). Understanding induced seismicity. *Science*, *354*(6318), 1380–1381. https://doi.org/10.1126/science.aal2584

Eyre, T. S., Eaton, D. W., Garagash, D. I., Zecevic, M., Venieri, M., Weir, R., & Lawton, D. C. (2019). The role of aseismic slip in hydraulic fracturing-induced seismicity. *Science Advances*, *5*(8), 1–11. https://doi.org/10.1126/sciadv.aav7172

Fagereng, Å., & Ikari, M. J. (2020). Low-temperature frictional characteristics of chlorite-epidote-amphibole assemblages: Implications for strength and seismic style of retrograde fault zones. *Journal of Geophysical Research: Solid Earth*, *125*, e2020JB019487. https://doi.org/10.1029/2020JB019487

Faulkner, D. R., Sanchez-Roa, C., Boulton, C., & den Hartog, S. A. M. (2018). Pore fluid pressure development in compacting fault gouge in theory, experiments, and nature. *Journal of Geophysical Research: Solid Earth*, *123*, 226–241. https://doi.org/10.1002/2017JB015130

Franz, G., & Liebscher, A. (2004). Physical and chemical properties of the epidote minerals-an introduction. *Reviews in Mineralogy and Geochemistry*, *56*(1), 1–81. https://doi.org/10.2138/gsrmg.56.1.1

Grapes, R. H., & Hoskin, P. W. O. (2004). Epidote group minerals in low-medium pressure metamorphic terranes. *Reviews in Mineralogy and Geochemistry*, *56*(1), 301–345. https://doi.org/10.2138/gsrmg.56.1.301

Grigoli, F., Cesca, S., Rinaldi, A. P., Manconi, A., López-Comino, J. A., Clinton, J. F., et al. (2018). The November 2017 Mw 5.5 Pohang earthquake: A possible case of induced seismicity in South Korea. *Science*, *369*(6392), 1003–1006. https://doi.org/10.1126/science.aat2010

Gu, J. C., Rice, J. R., Ruina, A. L., & Tse, S. T. (1984). Slip motion and stability of a single degree of freedom elastic system with rate and state dependent friction. *Journal of the Mechanics and Physics of Solids*, *32*(3), 167–196. https://doi.org/10.1016/0022-5096(84)90007-3

Guglielmi, Y., Elsworth, D., Cappa, F., Henry, P., Gout, C., Dick, P., Durand, J. C. (2015). In situ observations on the coupling between hydraulic diffusivity and displacements during fault reactivation in shales. *Journal of Geophysical Research: Solid Earth*, *120*(11), 7729–7748. https://doi.org/10.1002/2015JB012158

He, C., Yao, W., Wang, Z., & Zhou, Y. (2006). Strength and stability of frictional sliding of gabbro gouge at elevated temperatures. *Tectonophysics*, *427*(1–4), 217–229. https://doi.org/10.1016/j.tecto.2006.05.023

Hu, H., Dai, L., Li, H., Hui, K., & Sun, W. (2017). Influence of dehydration on the electrical conductivity of epidote and implications for high-conductivity anomalies in subduction zones. *Journal of Geophysical Research: Solid Earth*, *122*(4), 2751–2762. https://doi.org/10.1002/2016JB013767

Kameda, J., Raimbourg, H., Kogure, T., & Kimura, G. (2011). Low-grade metamorphism around the down-dip limit of seismogenic subduction zones: Example from an ancient accretionary complex in the Shimanto Belt, Japan. *Tectonophysics*, *502*(3–4), 383–392. https://doi.org/10.1016/j.tecto.2011.02.010

Kim, K. H., Ree, J. H., Kim, Y. H., Kim, S., Kang, S. Y., & Seo, W. (2018). Assessing whether the 2017 Mw 5.4 Pohang earthquake in South Korea was an induced event. *Science*, *360*(6392), 1007–1009. https://doi.org/10.1126/science.aat6081

Kolawole, F., Johnston, C. S., Morgan, C. B., Chang, J. C., Marfurt, K. J., Lockner, D. A., et al. (2019). The susceptibility of Oklahoma's basement to seismic reactivation. *Nature Geoscience*, *12*, 839–844. https://doi.org/10.1038/s41561-019-0440-5

Kwon, S., Xie, L., Park, S., Kim, K. I., Min, K. B., Kim, K. Y., et al. (2019). Characterization of 4.2-km-deep fractured granodiorite cores from Pohang geothermal reservoir, Korea. *Rock Mechanics and Rock Engineering*, *52*(3), 771–782. https://doi.org/10.1007/s00603-018-1639-2

Lee, K.-K., Ellsworth, W. L., Giardini, D., Townend, J., Ge, S., Shimamoto, T., et al. (2019). Managing injection-induced seismic risks. *Science*, *364*(6442), 730–732. https://doi.org/10.1126/science.aax1878

Lee, K.-K., Yeo, I.-W., Lee, J.-Y., Kang, T.-S., Rhie, J., Sheen, D.-H., et al. (2019). *Summary report of the Korean Government Commission on relations between the 2017 Pohang earthquake and EGS project*. Geological Society of Korea and Korean Government Commission on the Cause of the Pohang Earthquake Retrieved from http://www.gskorea.or.kr/custom/27/data/Summary_Report_on_Pohang_Earthquake_March_20_2019.pdf

Liou, J. G. (1993). Stabilities of natural epidotes. *Proceedings of a Symposium held in Neukirchen am Großvenediger (Salzburg/Austria)*, *49*, 7–16.

Lockner, D. A., Summers, R., & Byerlee, J. D. (1986). Effects of temperature and sliding rate on frictional strength of granite. *Pure and Applied Geophysics*, *124*(3), 445–469. https://doi.org/10.1007/BF00877211

Logan, J. M., Dengo, C. A., Higgs, N. G., & Wang, Z. Z. (1992). Fabrics of experimental fault zones: Their development and relationship to mechanical behavior. In B. Evans, & T.-F. Wong (Eds.), *Fault mechanics and transport properties of rocks* (pp. 33–67). Academic Press. https://doi.org/10.1016/S0074-6142(08)62814-4

Majer, E. L., Baria, R., Stark, M., Oates, S., Bommer, J., Smith, B., & Asanuma, H. (2007). Induced seismicity associated with enhanced geothermal systems. *Geothermics*, *36*(3), 185–222. https://doi.org/10.1016/j.geothermics.2007.03.003

Marone, C. (1998). Laboratory-derived friction laws and their application to seismic faulting. *Annual Review of Earth and Planetary Sciences*, *26*(1), 643–696. https://doi.org/10.1146/annurev.earth.26.1.643

McGarr, A., Simpson, D., & Seeber, L. (2002). 40-Case histories of induced and triggered seismicity. *International Geophysics*, *81*(Part A), 647–661. https://doi.org/10.1016/S0074-6142(02)80243-1

Mitchell, E. K., Fialko, Y., & Brown, K. M. (2016). Velocity-weakening behavior of Westerly granite at temperature up to 600°C. *Journal of Geophysical Research: Solid Earth*, *121*(9), 6932–6946. https://doi.org/10.1002/2016JB013081

Moore, D. E., Hickman, S., Lockner, D. A., & Dobson, P. F. (2001). Hydrothermal minerals and microstructures in the Silangkitang geothermal field along the Great Sumatran fault zone, Sumatra, Indonesia. *The Geological Society of America Bulletin*, *113*(9), 1179–1192. https://doi.org/10.1130/0016-7606(2001)113<1179:hmamit>2.0.co;2

Moore, D. E., & Lockner, D. A. (2008). Talc friction in the temperature range 25°-400°C: Relevance for fault-zone weakening. *Tectonophysics*, *449*, 120–132. https://doi.org/10.1016/j.tecto.2007.11.039

Moore, D. E., & Lockner, D. A. (2011). Frictional strengths of talc-serpentine and talc-quartz mixtures. *Journal of Geophysical Research: Solid Earth*, *116*(1). https://doi.org/10.1029/2010JB007881

Niemeijer, A. R., & Spiers, C. J. (2007). A microphysical model for strong velocity weakening in phyllosilicate-bearing fault gouges. *Journal of Geophysical Research: Solid Earth*, *112*(10), 1–12. https://doi.org/10.1029/2007JB005008

Niemeijer, A. R., & Vissers, R. L. (2014). Earthquake rupture propagation inferred from the spatial distribution of fault rock frictional properties. *Earth and Planetary Science Letters*, *396*, 154–164. https://doi.org/10.1016/j.epsl.2014.04.010

Olasolo, P., Juárez, M. C., Morales, M. P., Damico, S., & Liarte, I. A. (2016). Enhanced geothermal systems (EGS): A review. *Renewable and Sustainable Energy Reviews*, *56*, 133–144. https://doi.org/10.1016/j.rser.2015.11.031

Park, S., Kim, K. I., Xie, L., Yoo, H., Meier, P., Kim, M., et al. (2020). Observations and analyses of the first two hydraulic stimulations in the Pohang geothermal development site, South Korea. *Geothermics*, *88*, 101905. https://doi.org/10.1016/j.geothermics.2020.101905

Pluymakers, A. M. H., Samuelson, J. E., Niemeijer, A. R., & Spiers, C. J. (2014). Effects of temperature and CO_2 on the frictional behavior of simulated anhydrite fault rock. *Journal of Geophysical Research: Solid Earth*, *119*, 8728–8747. https://doi.org/10.1002/2014JB011575

Ruina, A. (1983). Slip instability and state variable friction laws. *Journal of Geophysical Research: Solid Earth*, *88*(B12), 10359–10370. https://doi.org/10.1029/JB088iB12p10359

Sawai, M., Niemeijer, A. R., Plümper, O., Hirose, T., & Spiers, C. J. (2016). Nucleation of frictional instability caused by fluid pressurization in subducted blueschist. *Geophysical Research Letters*, *43*(6), 2543–2551. https://doi.org/10.1002/2015GL067569

Schultz, R., Skoumal, R. J., Brudzinski, M. R., Eaton, D., Ellsworth, W., & Ellsworth, W. (2020). Hydraulic fracturing induced seismicity. *Reviews of Geophysics*, *58*(3), e2019RG000695. https://doi.org/10.1029/2019RG000695

Shapiro, S. A., Dinske, C., & Rothert, E. (2006). Hydraulic-fracturing controlled dynamics of microseismic clouds. *Geophysical Research Letters*, *33*(14), L14312. https://doi.org/10.1029/2006GL026365

Suckale, J. (2009). Induced seismicity in hydrocarbon fields. *Advances in Geophysics*, *51*(C), 55–106. https://doi.org/10.1016/S0065-2687(09)05107-3

Verberne, B. A., He, C., & Spiers, C. J. (2010). Frictional properties of sedimentary rocks and natural fault gouge from the Longmenshan fault zone, Sichuan, China. *Bulletin of the Seismological Society of America*, *100*(5B), 2767–2790. https://doi.org/10.1785/0120090287

Wehrens, P., Berger, A., Peters, M., Spillmann, T., & Herwegh, M. (2016). Deformation at the frictional-viscous transition: Evidence for cycles of fluid-assisted embrittlement and ductile deformation in the granitoid crust. *Tectonophysics*, *693*, 66–84. https://doi.org/10.1016/j.tecto.2016.10.022

Westaway, R., & Burnside, N. M. (2019). Fault "corrosion" by fluid injection: A potential cause of the November 2017 Mw 5.5 Korean earthquake. *Geofluids*, *2019*, 1–23. https://doi.org/10.1155/2019/1280721

Yeo, I. W., Brown, M., Ge, S., & Lee, K. K. (2020). Causal mechanism of injection-induced earthquakes through the Mw 5.5 Pohang earthquake case study. *Nature Communications*, *11*(1), 2614. https://doi.org/10.1038/s41467-020-16408-0

Zhang, C., Hu, S., Zhang, S., Li, S., Zhang, L., Kong, Y., et al. (2020). Radiogenic heat production variations in the Gonghe basin, northeastern Tibetan plateau: Implications for the origin of high-temperature geothermal resources. *Renewable Energy*, *148*, 284–297. https://doi.org/10.1016/j.renene.2019.11.156